

A high-entropy silicide: $(\text{Mo}_{0.2}\text{Nb}_{0.2}\text{Ta}_{0.2}\text{Ti}_{0.2}\text{W}_{0.2})\text{Si}_2$

Joshua Gild ^a, Jeffrey Braun ^b, Kevin Kaufmann ^c, Eduardo Marin ^c, Tyler Harrington ^a,
Patrick Hopkins ^b, Kenneth Vecchio ^{a,c}, Jian Luo ^{a,c,*}



^a Program of Materials Science and Engineering, University of California, San Diego, La Jolla, CA, 92093-0418, USA

^b Department of Mechanical and Aerospace Engineering, University of Virginia, Charlottesville, VA, 22904, USA

^c Department of NanoEngineering, University of California, San Diego, La Jolla, CA, 92093-0448, USA

ARTICLE INFO

Article history:

Received 8 February 2019

Received in revised form

10 March 2019

Accepted 13 March 2019

Available online 22 March 2019

Keywords:

High-entropy ceramics

High-entropy silicide

Thermal conductivity

Hardness

C40 crystal structure

ABSTRACT

A high-entropy metal disilicide, $(\text{Mo}_{0.2}\text{Nb}_{0.2}\text{Ta}_{0.2}\text{Ti}_{0.2}\text{W}_{0.2})\text{Si}_2$, has been successfully synthesized. X-ray diffraction (XRD), energy dispersive X-ray spectroscopy (EDX), and electron backscatter diffraction (EBSD) collectively show the formation of a single high-entropy silicide phase. This high-entropy $(\text{Mo}_{0.2}\text{Nb}_{0.2}\text{Ta}_{0.2}\text{Ti}_{0.2}\text{W}_{0.2})\text{Si}_2$ possesses a hexagonal C40 crystal structure with ABC stacking sequence and a space group of P6₂22. This discovery expands the known families of high-entropy materials from metals, oxides, borides, carbides, and nitrides to a silicide, for the first time to our knowledge, as well as demonstrating that a new, non-cubic, crystal structure (with lower symmetry) can be made into high-entropy phase. This $(\text{Mo}_{0.2}\text{Nb}_{0.2}\text{Ta}_{0.2}\text{Ti}_{0.2}\text{W}_{0.2})\text{Si}_2$ exhibits high nanohardness of 16.7 ± 1.9 GPa and Vickers hardness of 11.6 ± 0.5 GPa. Moreover, it has a low thermal conductivity of $6.9 \pm 1.1 \text{ W m}^{-1} \text{ K}^{-1}$, which is approximately one order of magnitude lower than that of the widely-used tetragonal MoSi_2 and $\sim 1/3$ of those reported values for the hexagonal NbSi_2 and TaSi_2 with the same crystal structure.

© 2019 The Chinese Ceramic Society. Production and hosting by Elsevier B.V. This is an open access article under the CC BY-NC-ND license (<http://creativecommons.org/licenses/by-nc-nd/4.0/>).

1. Introduction

Research on high-entropy alloys (HEAs), also known as multiple principal element alloys (MPEAs) or complex concentrated alloys (CCAs), has attracted considerable interest in the last ~15 years due to their unique properties and large compositional space for engineering [1–8]. A majority of the metallic HEAs adopt the simple face-centered cubic (FCC) or body-centered cubic (BCC) crystal structures, and a few hexagonal close packed (HCP) HEAs have been made [1–8].

Only in the last ~3.5 years have the ceramic counterparts to the metallic HEAs, or “high-entropy ceramics,” been successfully fabricated in bulk forms. In 2015, Rost et al. reported an entropy-stabilized oxide, $(\text{Mg}_{0.2}\text{Ni}_{0.2}\text{Co}_{0.2}\text{Cu}_{0.2}\text{Zn}_{0.2})\text{O}$, of a rocksalt structure (with a FCC Bravais lattice) [9]. In 2016, high-entropy metal diborides, e.g. $(\text{Hf}_{0.2}\text{Zr}_{0.2}\text{Ta}_{0.2}\text{Nb}_{0.2}\text{Ti}_{0.2})\text{B}_2$, were reported as a new class of ultra-high temperature ceramics (UHTCs) and the first high-entropy borides (as well as the first non-oxide high-entropy

ceramics made in the bulk form) [10]. Subsequently, the research on high-entropy ceramics has made rapid advances and attracted increasing attention. First, the high-entropy (entropy-stabilized) rocksalt oxides have been studied extensively due to their great potential as functional materials with low thermal conductivities [11–13] and colossal dielectric constants [14], as well as their potential applications in lithium-ion batteries [15,16]. Second, high-entropy metal diborides have also been studied by many groups as a new class of promising structural ceramics with increased hardness [17–19]; this line of work has further stimulated the subsequent development of high-entropy metal carbides as another class of UHTCs with increased hardness by various groups worldwide [20–29]. Third, several other classes of high-entropy ceramics have also been reported, including perovskite [30–32], spinel [33], defective fluorite-structured [34,35], and rare earth [32,36] oxides, as well as high-entropy nitrides [37,38]. It is worth noting that the high-entropy oxides [30–32,34–36], carbides [20–29], and nitrides [37,38] discovered to date all have cubic crystal structures with high symmetries. The only exception is the high-entropy metal diborides, which have a hexagonal (AlB_2) crystal structure, yet with a rather high symmetry (P6/mmm) [9].

As an increasing number of high-entropy oxides [30–32,34–36], borides [10,17–19], carbides [20–29], and nitrides [37,38] have been discovered, this study first reports, to the best of

* Corresponding author. University of California, San Diego, La Jolla, CA, 92093-0418, USA.

E-mail address: jluo@alum.mit.edu (J. Luo).

Peer review under responsibility of The Chinese Ceramic Society.

our knowledge, the synthesis and characterization of a high-entropy silicide: $(\text{Mo}_{0.2}\text{Nb}_{0.2}\text{Ta}_{0.2}\text{Ti}_{0.2}\text{W}_{0.2})\text{Si}_2$. Moreover, this $(\text{Mo}_{0.2}\text{Nb}_{0.2}\text{Ta}_{0.2}\text{Ti}_{0.2}\text{W}_{0.2})\text{Si}_2$ possesses a CrSi_2 -type hexagonal C40 structure with the ABC stacking sequence (Fig. 1); it represents a more complex crystal structure (with a lower $\text{P}6_2\text{2}2$ symmetry) in comparison with those reported in prior studies, thereby extending the state of the art for the discovery of new high-entropy materials.

In general, refractory disilicides, particularly MoSi_2 , are of great interest for high-temperature applications [39–45]. In this study, we have also examined the properties of this new high-entropy $(\text{Mo}_{0.2}\text{Nb}_{0.2}\text{Ta}_{0.2}\text{Ti}_{0.2}\text{W}_{0.2})\text{Si}_2$, showing high hardness ($16.7 \pm 1.9 \text{ GPa}$ nanohardness and $11.6 \pm 0.5 \text{ GPa}$ Vickers hardness) and much reduced thermal conductivity ($6.9 \pm 1.1 \text{ W m}^{-1} \text{ K}^{-1}$).

2. Experimental procedure

Powders of MoSi_2 , NbSi_2 , TaSi_2 , TiSi_2 , WSi_2 , and ZrSi_2 (99% purity, $\geq 45 \mu\text{m}$; Alfa Aesar) were utilized as starting materials. The raw powders were mixed via high-energy ball milling (HEBM) utilizing a SPEX 8000D mill for 6 h in a silicon nitride jar with silicon nitride media. Heptane was used to create a slurry for grinding to prevent caking of the powders and to minimize oxidation in the milling containers. The HEBM was done in 30-min intervals, interrupted by 10-min resting pauses to avoid overheating. The powders were then densified into 20-mm diameter disks via spark plasma sintering (SPS, Thermal Technologies, CA, USA) at 1650°C for 10 min under a uniaxial pressure of 50 MPa; then the pressure was

immediately reduced to 10 MPa at a rate of 40 MPa/min at 1650°C to minimize creep. The chamber was initially pumped down to vacuum of at least 20 mTorr and backfilled with argon for three times prior to the SPS experiments to minimize oxidation and a vacuum was maintained throughout the sintering process. The graphite die was lined with 125 μm thick graphite paper to prevent reaction of the specimen with the die.

The silicide was characterized by X-ray diffraction (XRD) utilizing a Rigaku diffractometer with $\text{Cu K}\alpha$ radiation. Scanning electron microscopy (SEM) was carried out, and the corresponding energy dispersive X-ray (EDX) spectroscopy compositional maps and electron backscatter diffraction (EBSD) maps were collected. The EDX measurements were performed at an e-beam voltage of 20 kV to examine the higher energy peaks of Hf, Ta, and W for minimal convolution of the peaks.

Hardness and modulus measurements were conducted via nano-indentation on a KLA-tenkor G200 Nanoindenter (KLA-tenkor, CA, USA). Nanohardness measurements were performed according to ISO 14577 under a load of 100 mN. In order to produce more statistically relevant data, the KLA-tenkor Express Test software module was employed to enable very large datasets to be generated. Vicker's hardness measurements were performed with a Vickers' diamond indenter at 200 kgf/mm^2 with a hold time of 15 s. The indentations were examined for conformation with the ASTM C1327. The indentations averaged 15–20 μm in width during the testing. Thirty measurements were performed at different locations of the specimen; the mean and standard deviation are reported. The Vickers indentation test was also carried out following the ASTM standard for measuring the microhardness.

Thermal conductivities were measured using time-domain thermoreflectance [46]. A thin Al transducer ($84 \pm 4 \text{ nm}$) is thermally evaporated onto the sample. Using a Ti:Sapphire laser emitting a train of $<200 \text{ fs}$ pulses at a central wavelength of 800 nm and a repetition rate of 80 MHz, the output is divided into a pump and probe path. The pump is modulated at 8.4 MHz to heat the sample, while the probe is used to measure the resulting change in temperature as a function of delay time out to 5.5 ns after pump absorption. The pump and probe $1/e^2$ diameters are 15 and 9 μm , respectively. The volumetric heat capacity was taken to be $2.5 \pm 3 \text{ J cm}^{-3} \text{ K}^{-1}$ based on the rule of mixtures average of constituent heat capacities [47].

3. Results and discussion

The XRD pattern shown in Fig. 2 suggests that the $(\text{Mo}_{0.2}\text{Nb}_{0.2}\text{Ta}_{0.2}\text{Ti}_{0.2}\text{W}_{0.2})\text{Si}_2$ specimen made by SPS possesses a hexagonal structure with the space group $\text{P}6_2\text{2}2$, or the CrSi_2 prototype structure. All peaks, except for one very minor peak, in the XRD pattern (Fig. 2) can be indexed to the hexagonal C40 structure with the ABC stacking sequence, as schematically illustrated in Fig. 1. SEM and EDX maps (Fig. 3) further demonstrated that this five-atom (Mo_{0.2}Nb_{0.2}Ta_{0.2}Ti_{0.2}W_{0.2})Si₂ specimen indeed formed a homogenous high-entropy solid solution. This hexagonal C40 structure was further confirmed by EBSD of a polished sample surface (Fig. 4). Lattice parameters of this $(\text{Mo}_{0.2}\text{Nb}_{0.2}\text{Ta}_{0.2}\text{Ti}_{0.2}\text{W}_{0.2})\text{Si}_2$ specimen were determined from the XRD to be: $a = 4.711 \text{ \AA}$ and $c = 6.522 \text{ \AA}$.

The formation of a hexagonal C40 crystal structure (with the ABC stacking sequence, as shown in Fig. 1) for this high-entropy $(\text{Mo}_{0.2}\text{Nb}_{0.2}\text{Ta}_{0.2}\text{Ti}_{0.2}\text{W}_{0.2})\text{Si}_2$ specimen is noteworthy and interesting since only two of the five constituent disilicides, NbSi_2 and TaSi_2 [44,48], form this hexagonal structure at high temperatures. TiSi_2 possesses an orthorhombic structure (with the ABCD stacking sequence) [49]. Both MoSi_2 and WSi_2 normally form tetragonal structures (with the AB stacking sequence), though the hexagonal

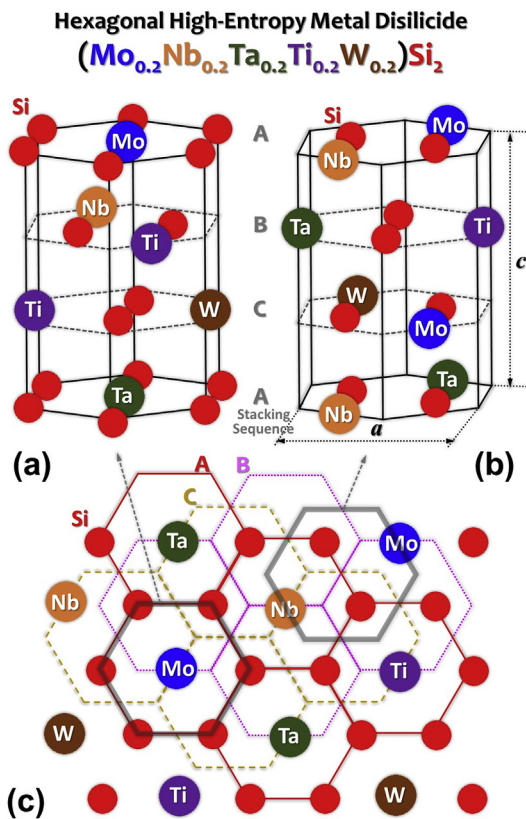


Fig. 1. Schematic illustration of the atomic structure of the hexagonal high-entropy disilicide with the ABC stacking sequences (i.e. the CrSi_2 prototype structure). Here, (a) and (b) are two alternative views of hexagonal cells (but not the unit cells) and (c) is an in-plane view, where the positions of both Si and metal atoms are shown for layer A while only the hexagonal Si nets are shown for layers B and C for clarity. The lattice parameters (a and c) are labeled. Noting that a is not the edge of the hexagonal cells shown in (a) and (b), but the distance between two metal cations within the layer.

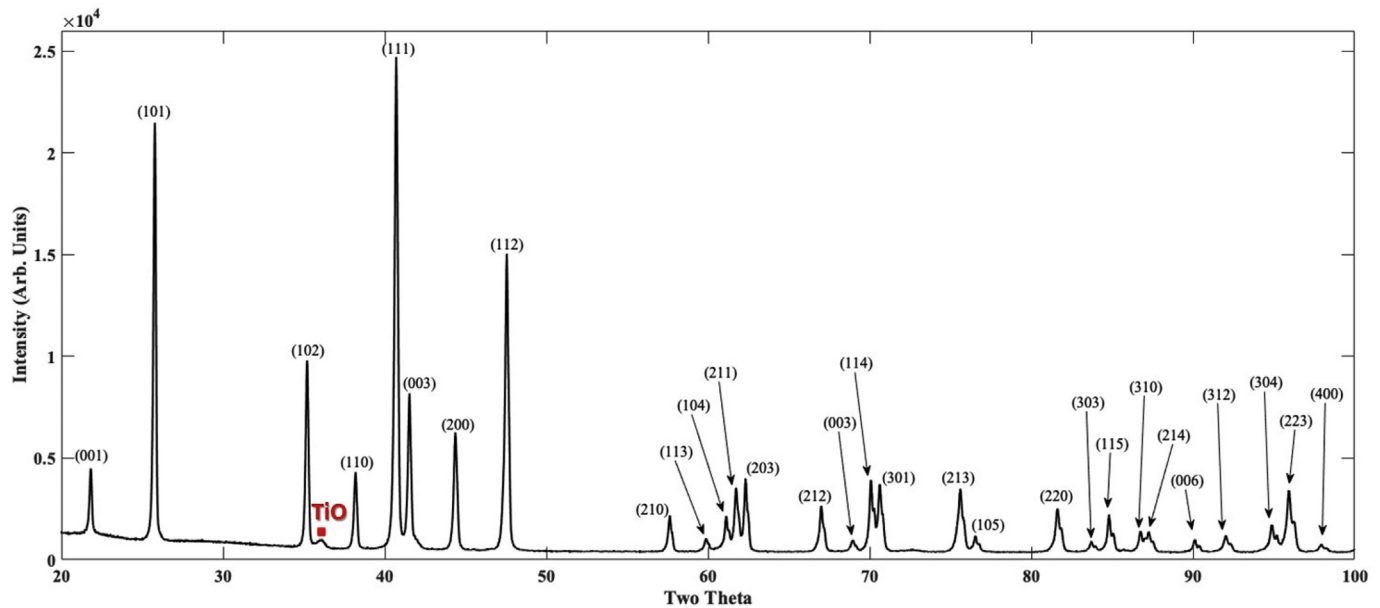


Fig. 2. XRD pattern of the $(\text{Mo}_{0.2}\text{Nb}_{0.2}\text{Ta}_{0.2}\text{Ti}_{0.2}\text{W}_{0.2})\text{Si}_2$ specimen. Except one minor peak from a secondary hexagonal TiO phase (labeled by the red solid square), all other XRD peaks are indexed to a hexagonal C40 structure (or the CrSi_2 prototype structure with the $\text{P}6_{2}22$ space group and the D_6 point group) with the lattice parameters $a = 4.711 \text{ \AA}$ and $c = 6.522 \text{ \AA}$.

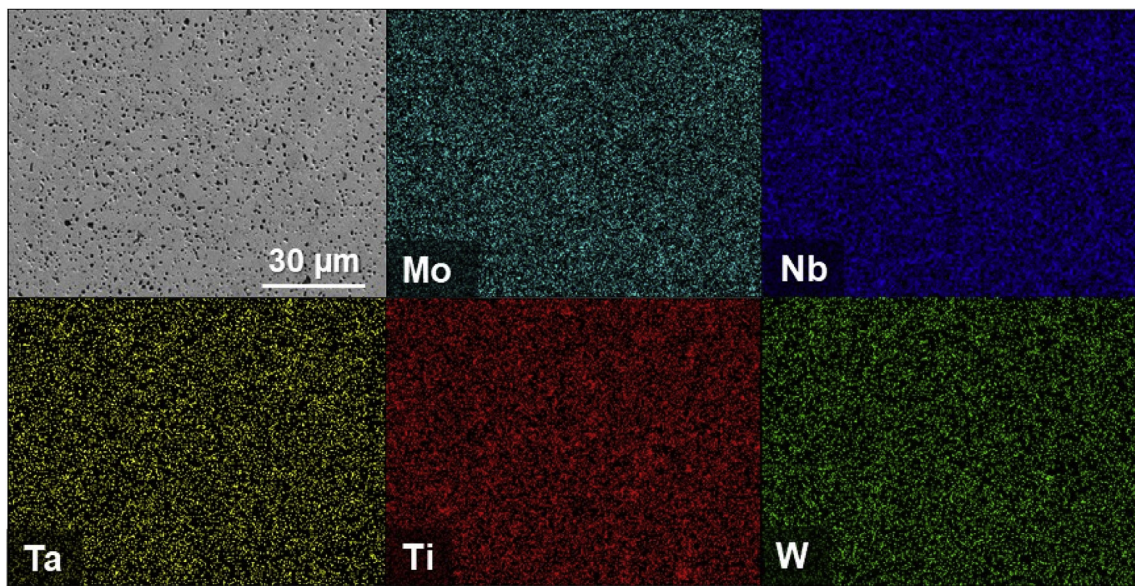


Fig. 3. SEM micrograph and the corresponding EDX elemental maps of the $(\text{Mo}_{0.2}\text{Nb}_{0.2}\text{Ta}_{0.2}\text{Ti}_{0.2}\text{W}_{0.2})\text{Si}_2$ specimen.

phases were observed at lower temperatures (below 900°C and 550°C , respectively) in thin films [48,50].

This $(\text{Mo}_{0.2}\text{Nb}_{0.2}\text{Ta}_{0.2}\text{Ti}_{0.2}\text{W}_{0.2})\text{Si}_2$ represents a new high-entropy ceramic made, with a new, and perhaps the lowest, symmetry among all high-entropy metals and ceramics reported. To date, all except for two high-entropy metals and ceramics reported have cubic symmetries (of simple FCC and BCC [1–8], rocksalt [9,20–29,37,38], fluorite [34,35], perovskite [30–32], and spinel [33] structures). The two other classes of non-cubic high-entropy materials reported are the metallic HCP HEAs (with the space group of $\text{P}6_3/\text{mmc}$) [8] and high-entropy metal borides (with the space group of $\text{P}6/\text{mmm}$) [10]. This high-entropy $(\text{Mo}_{0.2}\text{Nb}_{0.2}\text{Ta}_{0.2}\text{Ti}_{0.2}\text{W}_{0.2})\text{Si}_2$ has a lower symmetry of $\text{P}6_{2}22$, with a more

complex ABC stacking sequence (Fig. 1).

It should be noted that a secondary TiO phase is also present, producing a minor XRD peak as indicated in Fig. 2. We assume that TiO formed because TiSi_2 possesses a melting point of $\sim 1500^\circ\text{C}$ [26,27], below our SPS temperature; thus, it is likely that TiSi_2 promoted the formation of a (transient) liquid phase that assisted sintering but captured surface oxides. TiSi_2 has been utilized for liquid assisted sintering of diborides in a similar manner [51,52]. The secondary oxide phases seen in the SEM image (the dark phase in the first panel of SEM image in Fig. 3) are likely SiO_2 -based glass, which did not show up in XRD (since the amount of TiO identified by XRD, as shown in Fig. 2, is small). ImageJ analysis of the SEM image was performed to estimate the high-entropy silicide phase to

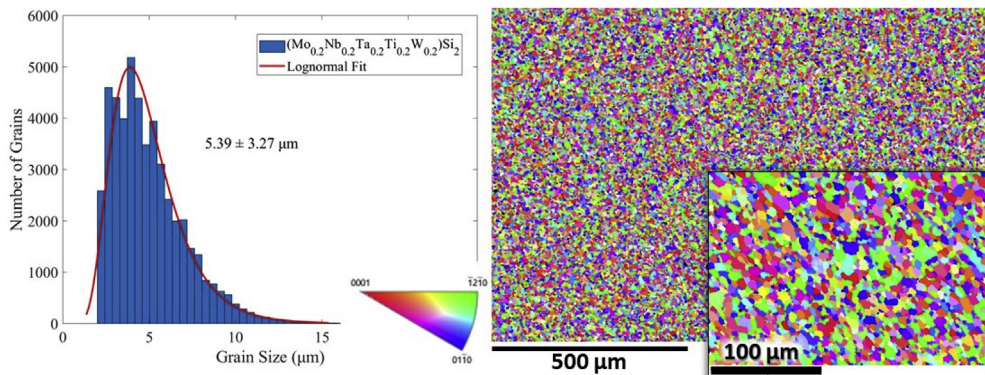


Fig. 4. EBSD map of $>1\text{ mm}^2$ area of the high-entropy $(\text{Mo}_{0.2}\text{Nb}_{0.2}\text{Ta}_{0.2}\text{Ti}_{0.2}\text{W}_{0.2})\text{Si}_2$ surface, showing a rather uniform microstructure. No significant texture was observed. The measured grain size distribution is given, which fits a lognormal curve. The inset on the right-bottom corner is an additional EBSD map taken at a higher magnification.

be approximately 89 vol %.

EBSD was utilized to measure the grain size and examine the texture of the sintered $(\text{Mo}_{0.2}\text{Nb}_{0.2}\text{Ta}_{0.2}\text{Ti}_{0.2}\text{W}_{0.2})\text{Si}_2$ specimen. An average grain size of $5.4 \pm 3.3\text{ }\mu\text{m}$ was found from a measurement of over 5000 grains. No significant texturing was evident in the sample. Two EBSD maps at low and high magnifications, an inverse pole figure, and the measured grain size distribution are shown in Fig. 4.

Nanoindentation hardness measurements of this (hexagonal) high-entropy $(\text{Mo}_{0.2}\text{Nb}_{0.2}\text{Ta}_{0.2}\text{Ti}_{0.2}\text{W}_{0.2})\text{Si}_2$ following the ISO 14577 standard using a load of 100 mN produced a value of $16.7 \pm 1.9\text{ GPa}$ with a large number of indents. It also measured an elastic modulus of $421 \pm 19\text{ GPa}$, in agreement with the measurements taken by Nakamura et al. for MoSi_2 and WSi_2 [53]. Moreover, we have conducted Vickers indentation test and measured a microhardness value of $11.6 \pm 0.5\text{ GPa}$ from our high-entropy $(\text{Mo}_{0.2}\text{Nb}_{0.2}\text{Ta}_{0.2}\text{Ti}_{0.2}\text{W}_{0.2})\text{Si}_2$ specimen. These measured hardness values are comparable to those reported for MoSi_2 in literature, with Newman et al. reporting up to $17.5 \pm 2.0\text{ GPa}$ in nanoindentation and Vickers hardness in other prior studies varying from approximately 9 to 14 GPa [53–57]. The microhardness value of our high-entropy $(\text{Mo}_{0.2}\text{Nb}_{0.2}\text{Ta}_{0.2}\text{Ti}_{0.2}\text{W}_{0.2})\text{Si}_2$ specimen is compared with five individual constituent metal disilicides in Table 1. Notably, the Vickers hardness of this high-entropy $(\text{Mo}_{0.2}\text{Nb}_{0.2}\text{Ta}_{0.2}\text{Ti}_{0.2}\text{W}_{0.2})\text{Si}_2$ specimen is higher than the average of the microhardness values of the five individual metal disilicides reported in the literature (which was calculated to be 9.32 GPa by taking a median value for MoSi_2).

A significantly reduced thermal conductivity was measured for this (hexagonal) high-entropy $(\text{Mo}_{0.2}\text{Nb}_{0.2}\text{Ta}_{0.2}\text{Ti}_{0.2}\text{W}_{0.2})\text{Si}_2$, in comparison with other metal disilicides [58,59]. Fitting a multilayer heat diffusion model to experimental ratio data [60], the best-fit thermal conductivity was determined to be $6.9 \pm 1.1\text{ W m}^{-1}\text{ K}^{-1}$. In comparison, the thermal conductivity of the (tetragonal) MoSi_2

has been measured to be $65\text{ W m}^{-1}\text{ K}^{-1}$ [58]. The thermal conductivities of (hexagonal) NbSi_2 , (hexagonal) TaSi_2 , (orthorhombic) TiSi_2 , and (tetragonal) WSi_2 , respectively were measured by Neshpor [59] to be $19.1\text{ W m}^{-1}\text{ K}^{-1}$, $21.9\text{ W m}^{-1}\text{ K}^{-1}$, $45.9\text{ W m}^{-1}\text{ K}^{-1}$, $46.6\text{ W m}^{-1}\text{ K}^{-1}$, respectively; these reported values from literature are listed in Table 1 to be compared with our measured thermal conductivity of the high-entropy $(\text{Mo}_{0.2}\text{Nb}_{0.2}\text{Ta}_{0.2}\text{Ti}_{0.2}\text{W}_{0.2})\text{Si}_2$. While it is possible that the presence of oxide contamination and porosity reduces the thermal conductivity of our specimen, the measured value of $6.9 \pm 1.1\text{ W m}^{-1}\text{ K}^{-1}$ is significantly lower than reported values of any of the five constituent disilicides. Noting that NbSi_2 and TaSi_2 , which have the same hexagonal crystal and lowest thermal conductivities of $19.1\text{ W m}^{-1}\text{ K}^{-1}$ and $21.9\text{ W m}^{-1}\text{ K}^{-1}$, respectively [59], among the five individual disilicides, are perhaps the best benchmarks for comparison. Still, the measured thermal conductivity of this high-entropy $(\text{Mo}_{0.2}\text{Nb}_{0.2}\text{Ta}_{0.2}\text{Ti}_{0.2}\text{W}_{0.2})\text{Si}_2$ is substantial lower ($\sim 1/3$), presumably due to the high phonon scattering from the five different cations with different masses and a highly distorted lattice. A prior modeling study has demonstrated that $>10\text{X}$ reduction in thermal conductivity can be achieved in high-entropy ceramics [13], and similar levels of thermal conductivity reduction was indeed observed in entropy-stabilized oxides [12].

We also attempted to fabricate a $(\text{Mo}_{0.2}\text{Nb}_{0.2}\text{Ta}_{0.2}\text{W}_{0.2}\text{Zr}_{0.2})\text{Si}_2$ specimen via the same procedure, but it did not form a single high-entropy phase. The measured XRD pattern and EDX elemental maps of this $(\text{Mo}_{0.2}\text{Nb}_{0.2}\text{Ta}_{0.2}\text{W}_{0.2}\text{Zr}_{0.2})\text{Si}_2$ specimen are shown in Fig. 5. While a primary hexagonal C40 phase did form, additional Ta-Zr-Si and Nb-Zr-Si rich secondary phases were observed.

4. Conclusions

A high-entropy metal disilicide, $(\text{Mo}_{0.2}\text{Nb}_{0.2}\text{Ta}_{0.2}\text{Ti}_{0.2}\text{W}_{0.2})\text{Si}_2$, was successfully synthesized. It possesses a hexagonal structure

Table 1

Comparison of the properties of the high-entropy $(\text{Mo}_{0.2}\text{Nb}_{0.2}\text{Ta}_{0.2}\text{Ti}_{0.2}\text{W}_{0.2})\text{Si}_2$ with five individual constituent metal disilicides.

Compound	Crystal Structure	Vickers Hardness (GPa)	Thermal Conductivity [$\text{W m}^{-1}\text{ K}^{-1}$]	References
MoSi_2	Tetragonal	9–14	65	[53,54,57]
NbSi_2	Hexagonal	5.4	19.1	[59,61,62]
TaSi_2	Hexagonal	13	21.9	[59,62,63]
TiSi_2	Orthorhombic	8.5	45.9	[59,62,64]
WSi_2	Tetragonal	8.2	46.6	[53,59,62,65]
Rule-of-mixture average of five metal disilicides		9.32	40	
$(\text{Mo}_{0.2}\text{Nb}_{0.2}\text{Ta}_{0.2}\text{Ti}_{0.2}\text{W}_{0.2})\text{Si}_2$	Hexagonal	11.6 ± 0.5	6.9 ± 1.1	This Study

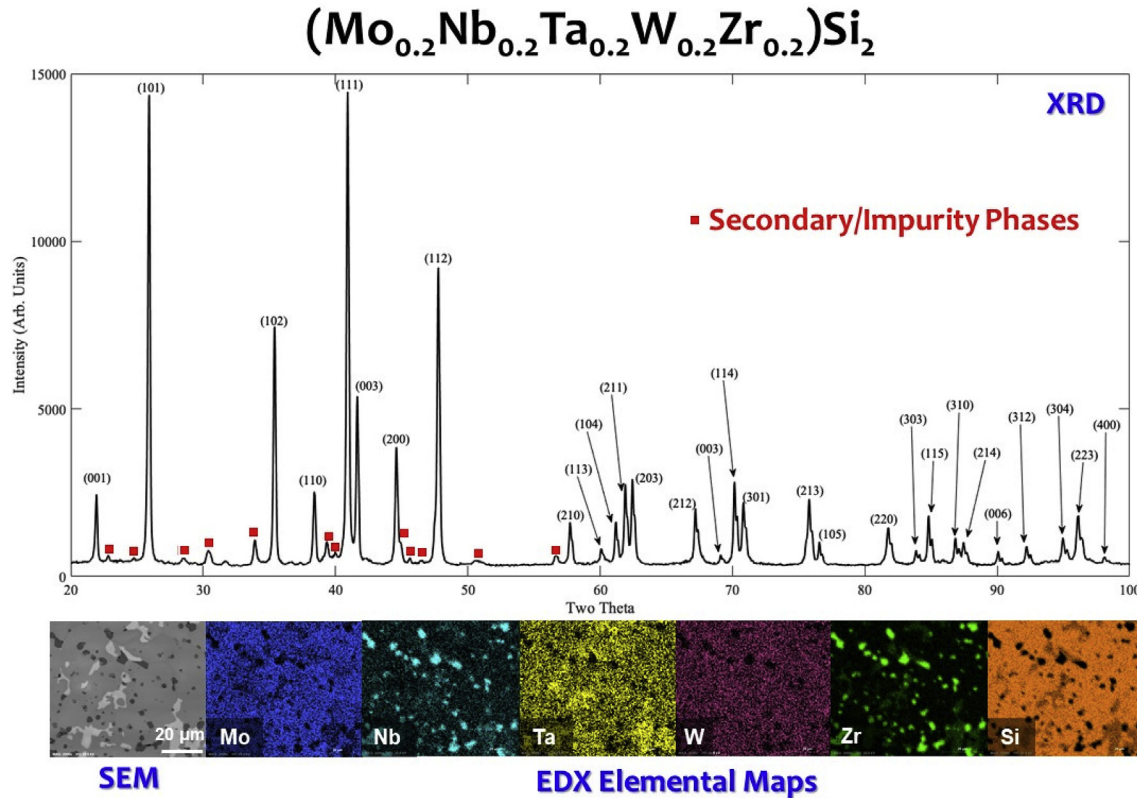


Fig. 5. XRD pattern, SEM micrograph, and the corresponding EDX elemental maps of the $(\text{Mo}_{0.2}\text{Nb}_{0.2}\text{Ta}_{0.2}\text{W}_{0.2}\text{Zr}_{0.2})\text{Si}_2$ specimen. In addition to a primary hexagonal C40 phase, Ta-Zr-Si and Nb-Zr-Si rich secondary phases were observed.

with a space group of $P6_222$, representing a new high-entropy material family (a high-entropy silicide) and a new non-cubic high-entropy crystal structure made. Characterization by XRD, EDX, and EBSD confirm the presence of a single high-entropy solid-solution phase, albeit some oxide contaminations.

This high-entropy $(\text{Mo}_{0.2}\text{Nb}_{0.2}\text{Ta}_{0.2}\text{Ti}_{0.2}\text{W}_{0.2})\text{Si}_2$ exhibits high nanohardness of 16.7 ± 1.9 GPa and Vickers hardness of 11.6 ± 0.5 GPa. The measured thermal conductivity of $(\text{Mo}_{0.2}\text{Nb}_{0.2}\text{Ta}_{0.2}\text{Ti}_{0.2}\text{W}_{0.2})\text{Si}_2$ is $6.9 \pm 1.1 \text{ W m}^{-1} \text{ K}^{-1}$, which is approximately one order of magnitude lower than that of the widely-used tetragonal MoSi_2 [58] and $\sim 1/3$ of those reported for the hexagonal NbSi_2 and TaSi_2 with the same crystal structure [59]. The significant reduction in the thermal conductivity can be explained from the high phonon scattering in the high-entropy ceramic.

Acknowledgement

We acknowledge the partial financial support from an Office of Naval Research MURI program (grant no. N00014-15-1-2863; Program Managers: Dr. Kenny Lipkowitz and Dr. Eric Wuchina). P.E.H. also appreciates funding from the National Science Foundation, Grant No. CBET-1706388. K. Kaufmann was supported by the Department of Defense (DoD) through the National Defense Science and Engineering Graduate Fellowship (NDSEG) program as well as the ARCS foundation.

References

- [1] Tsai M-H, Yeh J-W. High-entropy alloys: a critical review. *Materials Research Letters* 2014;2:107–23. <https://doi.org/10.1080/21663831.2014.912690>.
- [2] Zhang Y, Zuo TT, Tang Z, Gao MC, Dahmen KA, Liaw PK, Lu ZP. Microstructures and properties of high-entropy alloys. *Prog Mater Sci* 2014;61:1–93. <https://doi.org/10.1016/j.pmatsci.2013.10.001>.
- [3] Murty BS, Yeh JW, Ranganathan S. High-entropy alloys. 2014.
- [4] Yeh J-W, Lin S-J, Chin T-S, Gan J-Y, Chen S-K, Shun T-T, Tsau C-H, Chou S-Y. Formation of simple crystal structures in Cu-Co-Ni-Cr-Al-Fe-Ti-V alloys with multiprincipal metallic elements. *Metall Mater Trans* 2004;35:2533–6.
- [5] Yeh JW, Chen SK, Lin SJ, Gan JY, Chin TS, Shun TT, Tsau CH, Chang SY. Nanostructured high-entropy alloys with multiple principal elements: novel alloy design concepts and outcomes. *Adv Eng Mater* 2004;6:299–303. <https://doi.org/10.1002/adem.200300567>.
- [6] Senkov ON, Miracle DB, Chaput KJ, Couzinie J-P. Development and exploration of refractory high entropy alloys—a review. *J Mater Res* 2018;33:3092–128. <https://doi.org/10.1557/jmr.2018.153>.
- [7] Cantor B, Chang I, Knight P, Vincent A. Microstructural development in equiatomic multicomponent alloys. *Mater Sci Eng, A* 2004;375:213–8.
- [8] Miracle DB, Senkov ON. A critical review of high entropy alloys and related concepts. *Acta Mater* 2017;122:448–511. <https://doi.org/10.1016/j.actamat.2016.08.081>.
- [9] Rost CM, Sachet E, Borman T, Maballegh A, Dickey EC, Hou D, Jones JL, Curtarolo S, Maria J-P. Entropy-stabilized oxides. *Nat Commun* 2015;6. <https://doi.org/10.1038/ncomms9485>.
- [10] Gild J, Zhang Y, Harrington T, Jiang S, Hu T, Quinn MC, Mellor WM, Zhou N, Vecchio K, Luo J. High-entropy metal diborides: a new class of high-entropy materials and a new type of ultrahigh temperature ceramics. *Sci Rep* 2016;6:37946. <https://doi.org/10.1038/srep37946>.
- [11] Giri A, Braun JL, Hopkins PE. Reduced dependence of thermal conductivity on temperature and pressure of multi-atom component crystalline solid solutions. *J Appl Phys* 2018;123:015106.
- [12] Braun JL, Rost CM, Lim M, Giri A, Olson DH, Kotsonis GN, Stan G, Brenner DW, Maria JP, Hopkins PE. Charge-induced disorder controls the thermal conductivity of entropy-stabilized oxides. *Adv Mater* 2018;30:1805004.
- [13] Giri A, Braun JL, Rost CM, Hopkins PE. On the minimum limit to thermal conductivity of multi-atom component crystalline solid solutions based on impurity mass scattering. *Scripta Mater* 2017;138:134–8.
- [14] Bérardan D, Franger S, Dragoe D, Meena AK, Dragoe N. Colossal dielectric constant in high entropy oxides. *Phys Status Solidi Rapid Res Lett* 2016;10: 328–33. <https://doi.org/10.1002/pssr.201600043>.
- [15] Sarkar A, Velasco L, Wang D, Wang Q, Talasila G, de Biasi L, Kübel C, Brezesinski T, Bhattacharya SS, Hahn H, Breitung B. High entropy oxides for reversible energy storage. *Nat Commun* 2018;9:3400. <https://doi.org/10.1038/s41467-018-05774-5>.

[16] Bérardan D, Franger S, Meena A, Dragoe N. Room temperature lithium superionic conductivity in high entropy oxides. *J Mater Chem* 2016;4: 9536–41.

[17] Tallarita G, Licheri R, Garroni S, Orrù R, Cao G. Novel processing route for the fabrication of bulk high-entropy metal diborides. *Scripta Mater* 2019;158: 100–4. <https://doi.org/https://doi.org/10.1016/j.scriptamat.2018.08.039>.

[18] Mansouri Tehrani A, Brgoch J. Hard and superhard materials: a computational perspective. *J Solid State Chem* 2019;271:47–58. <https://doi.org/https://doi.org/10.1016/j.jssc.2018.10.048>.

[19] Mayrhofer PH, Kirnbauer A, Ertelthaler P, Koller CM. High-entropy ceramic thin films: A case study on transition metal diborides. *Scripta Mater* 2018;149:93–7.

[20] Harrington TJ, Gild J, Sarker P, Toher C, Rost CM, Dippo OF, McElfresh C, Kaufmann K, Marin E, Borowski L, Hopkins PE, Luo J, Curtarolo S, Brenner DW, Vecchio KS. Phase stability and mechanical properties of novel high entropy transition metal carbides. *Acta Mater* 2019;166:271–80. <https://doi.org/https://doi.org/10.1016/j.actamat.2018.12.054>.

[21] Zhou J, Zhang J, Zhang F, Niu B, Lei L, Wang W. High-entropy carbide: a novel class of multicomponent ceramics. *Ceram Int* 2018;44:22014–8. <https://doi.org/https://doi.org/10.1016/j.ceramint.2018.08.100>.

[22] Yan X, Constantin L, Lu Y, Silvain J-F, Nastasi M, Cui B. Hf_{0.2}Zr_{0.2}Ta_{0.2}Nb_{0.2}Ti_{0.2}C high-entropy ceramics with low thermal conductivity. *J Am Ceram Soc* 2018;101:4486–91. <https://doi.org/10.1111/jace.15779>.

[23] Sarker P, Harrington T, Toher C, Oses C, Samiee M, Maria J-P, Brenner DW, Vecchio KS, Curtarolo S. High-entropy high-hardness metal carbides discovered by entropy descriptors. *Nat Commun* 2018;9:4980. <https://doi.org/10.1038/s41467-018-07160-7>.

[24] Castle E, Csanádi T, Grasso S, Dusza J, Reece M. Processing and properties of high-entropy ultra-high temperature carbides. *Sci Rep* 2018;8:8609.

[25] Dusza J, Švec P, Girman V, Sedlák R, Castle EG, Csanádi T, Kovalčíková A, Reece MJ. Microstructure of (Hf-Ta-Zr-Nb) C high-entropy carbide at micro and nano/atomic level. *J Eur Ceram Soc* 2018;38:4303–7.

[26] Demirskyi D, Borodianska H, Suzuki T, Sakka Y, Yoshimi K, Vasylkiv O. High-temperature flexural strength performance of ternary high-entropy carbide consolidated via spark plasma sintering of TaC, ZrC and NbC. *Scripta Mater* 2019;164:12–6.

[27] Yang Y, Wang W, Gan G-Y, Shi X-F, Tang B-Y. Structural, mechanical and electronic properties of (TaNbHfTiZr) C high entropy carbide under pressure: Ab initio investigation. *Phys B Condens Matter* 2018;550:163–70.

[28] Ye B, Wen T, Huang K, Wang CZ, Chu Y. First-principles study, fabrication and characterization of (Hf_{0.2}Zr_{0.2}Ta_{0.2}Nb_{0.2}Ti_{0.2}) C high-entropy ceramic. *J Am Ceram Soc* 2019;00:1–9. <https://doi.org/10.1111/jace.16295>.

[29] Feng L, Fahrenholtz WG, Hilmas GE, Zhou Y. Synthesis of single-phase high-entropy carbide powders. *Scripta Mater* 2019;162:90–3.

[30] Jiang S, Hu T, Gild J, Zhou N, Nie J, Qin M, Harrington T, Vecchio K, Luo J. A new class of high-entropy perovskite oxides. *Scripta Mater* 2018;142:116–20.

[31] Sharma Y, Musico BL, Gao X, Hua C, May AF, Herklotz A, Rastogi A, Mandrus D, Yan J, Lee HN. Single-crystal high entropy perovskite oxide epitaxial films. *Physical Review Materials* 2018;2:060404.

[32] Sarker A, Djenadic R, Wang D, Hein C, Kautenburger R, Clemens O, Hahn H. Rare earth and transition metal based entropy stabilised perovskite type oxides. *J Eur Ceram Soc* 2018;38:2318–27. <https://doi.org/https://doi.org/10.1016/j.jeurceramsoc.2017.12.058>.

[33] Dąbrowa J, Stygar M, Mikula A, Knapik A, Mroczka K, Tejchman W, Dzielewski M, Martin M. Synthesis and microstructure of the (Co, Cr, Fe, Mn, Ni)₃O₄ high entropy oxide characterized by spinel structure. *Mater Lett* 2017;216:32–6.

[34] Gild J, Samiee M, Braun JL, Harrington T, Vega H, Hopkins PE, Vecchio K, Luo J. High-entropy fluorite oxides. *J Eur Ceram Soc* 2018;38:3578–84.

[35] Chen K, Pei X, Tang L, Cheng H, Li Z, Li C, Zhang X, An L. A five-component entropy-stabilized fluorite oxide. *J Eur Ceram Soc* 2018;38:4161–4.

[36] Djenadic R, Sarker A, Clemens O, Lohr C, Botros M, Chakravadhanula VS, Kübel C, Bhattacharya SS, Gandhi AS, Hahn H. Multicomponent equiatomic rare earth oxides. *Materials Research Letters* 2017;5:102–9.

[37] Jin T, Sang X, Unocic RR, Kinch RT, Liu X, Hu J, Liu H, Dai S. Mechanochemical-assisted synthesis of high-entropy metal nitride via a soft urea strategy. *Adv Mater* 2018;30:1707512.

[38] Braic V, Vladescu A, Balaceanu M, Luculescu CR, Braic M. Nanostructured multi-element (TiZrNbHfTa)N and (TiZrNbHfTa)C hard coatings. *Surf Coatings Technol* 2012;211:117–21. <https://doi.org/https://doi.org/10.1016/j.surcoat.2011.09.033>.

[39] Petrovic JJ. MoSi₂-based high-temperature structural silicides. *MRS Bull* 1993;18:35–41.

[40] Petrovic JJ, Vasudevan A. Overview of high temperature structural silicides. *MRS Online Proceedings Library Archive* 1993;322.

[41] Petrovic JJ. Mechanical behavior of MoSi₂ and MoSi₂ composites. *Mater Sci Eng, A* 1995;192:31–7.

[42] Raj S. A preliminary assessment of the properties of a chromium silicide alloy for aerospace applications. *Mater Sci Eng, A* 1995;192:583–9.

[43] Samsonov G, Lavrenko V, Glebov L. Oxidation of chromium disilicide in oxygen. *Sov Powder Metall Met Ceram* 1974;13:36–8.

[44] Song B, Feng P, Wang J, Ge Y, Wu G, Wang X, Akhtar F. Oxidation properties of self-propagating high temperature synthesized niobium disilicide. *Corros Sci* 2014;85:311–7.

[45] Yao Z, Stiglich J, Sudarshan T. Molybdenum silicide based materials and their properties. *J Mater Eng Perform* 1999;8:291–304.

[46] Jiang P, Qian X, Yang R. Tutorial: time-domain thermoreflectance (TDTR) for thermal property characterization of bulk and thin film materials. *J Appl Phys* 2018;124:161103.

[47] Touloukian Y, Makita M. Plenum. 1976. New York.

[48] d'Hourle F, Petersson C, Tsai M. Observations on the hexagonal form of MoSi₂ and WSi₂ films produced by ion implantation and on related snowplow effects. *J Appl Phys* 1980;51:5976–80.

[49] Jeitschko W. Refinement of the crystal structure of TiSi₂ and some comments on bonding in TiSi₂ and related compounds. *Acta Crystallogr B Struct Crystalllogr Cryst Chem* 1977;33:2347–8.

[50] Murarka S, Read M, Chang C. Hexagonal WSi₂ in cosputtered (tungsten and silicon) mixture. *J Appl Phys* 1981;52:7450–2.

[51] Sonber J, Murthy TC, Subramanian C, Kumar S, Fotedar R, Suri A. Investigations on synthesis of ZrB₂ and development of new composites with HfB₂ and TiSi₂. *Int J Refract Metals Hard Mater* 2011;29:21–30.

[52] Raju GB, Basu B. Densification, sintering reactions, and properties of titanium diboride with titanium disilicide as a sintering aid. *J Am Ceram Soc* 2007;90: 3415–23.

[53] Nakamura M, Matsumoto S, Hirano T. Elastic constants of MoSi₂ and WSi₂ single crystals. *J Mater Sci* 1990;25:3309–13.

[54] Newman A, Jewett T, Sampath S, Berndt C, Herman H. Indentation response of molybdenum disilicide. *J Mater Res* 1998;13:2662–71.

[55] Haji-Mahmood M, Chumbley L. Processing and characterization of nanocrystalline molybdenum disilicide consolidated by hot isostatic pressing (HIP). *Nanostruct Mater* 1996;7:95–112.

[56] Schwarz R, Srinivasan S, Petrovic JJ, Maggiore C. Synthesis of molybdenum disilicide by mechanical alloying. *Mater Sci Eng, A* 1992;155:75–83.

[57] Wade RK, Petrovic JJ. Processing temperature effects on molybdenum disilicide. *J Am Ceram Soc* 1992;75:3160–2.

[58] Vasudevan A, Petrovic J. A comparative overview of molybdenum disilicide composites. *Mater Sci Eng, A* 1992;155:1–17.

[59] Neshop V. The thermal conductivity of the silicides of transition metals. *J Eng Phys Thermophys* 1968;15:750–2.

[60] Cahill DG. Analysis of heat flow in layered structures for time-domain thermoreflectance. *Rev Sci Instrum* 2004;75:5119–22.

[61] Yazdani Z, Karimzadeh F, Abbasi M-H. Characterization of nanostructured NbSi₂ intermetallic coatings obtained by plasma spraying of mechanically alloyed powders. *J Therm Spray Technol* 2015;24:947–52.

[62] Vorotil S, Potanin AY, Iatsyuk IV, Levashev EA. SHS of silicon-based ceramics for the high-temperature applications. *Adv Eng Mater* 2018;20:1800200.

[63] Shon I-J, Ko I-Y, Chae S-M, Na K-i. Rapid consolidation of nanostructured TaSi₂ from mechanochemically synthesized powder by high frequency induction heated sintering. *Ceram Int* 2011;37:679–82.

[64] Frommeyer G, Rosenkranz R. In metallic Materials with high structural efficiency 287–308. Springer; 2004.

[65] Shon I, Rho D, Kim H, Munir Z. Dense WSi₂ and WSi₂–20 vol.% ZrO₂ composite synthesized by pressure-assisted field-activated combustion. *J Alloy Comp* 2001;322:120–6.



Joshua Gild is a PhD candidate at the University of California, San Diego in the Program of Materials Science and Engineering. He holds a B.S. in Physics from Boston College and a M.S. in Materials Science and Engineering from the Rochester Institute of Technology. His current research focuses on the fabrication of new classes of high-entropy ultra-high temperature ceramics. His research efforts have encompassed refractory diborides, fluorite type oxides, and refractory disilicides.



Kevin Kaufmann is a PhD student in NanoEngineering at the University of California, San Diego. He is a fellow in the National Defense Science and Engineering Graduate (NDSEG) Fellowship Program. He holds Masters and Bachelor degrees in NanoEngineering. Kaufmann was awarded the National Science Foundation (NSF) graduate student fellowship in 2017. He was also awarded the Abe Hurlich Scholarship from the San Diego Chapter of American Society of Minerals International in 2018 for his exemplary work in materials design and developing new analysis techniques. Kaufmann's research has been featured in interviews by various media and radio groups including BBC Newsday, BBC NewsHour, and *Biotechniques*.



Patrick E. Hopkins received his Ph.D. in mechanical and aerospace engineering from the University of Virginia in 2008, following a B.S. degree in mechanical engineering and the B.A. degree in physics at the University of Virginia in 2004. He spent three years as a Harry S. Truman Postdoctoral Fellow at Sandia National Laboratories in Albuquerque, NM, USA, from 2008 to 2011. He began a faculty appointment at the University of Virginia in December 2011 as an Assistant Professor, was promoted to Associate Professor with tenure in August 2015, and Professor with tenure in August 2018. Dr. Hopkins is a recipient of the Air Force Office of Scientific Research and Office of Naval Research Young Investigator Awards, the American Society of Mechanical Engineers Bergles–Rohsenow Young Investigator Award in Heat Transfer, the Presidential Early Career Award for Scientists and Engineers (PECASE), and is a Fellow of the American Society of Mechanical Engineers.



Jian Luo graduated from Tsinghua University with dual Bachelor's degrees. After receiving his Ph.D. degree from M.I.T. in 2001, Luo worked in the industry for more than two years with Lucent Technologies and OFS/Fitel. In 2003, he joined the Clemson faculty, where he served as an Assistant/Associate/Full Professor of Materials Science and Engineering. In 2013, he moved to UCSD as a Professor of NanoEngineering and Professor of Materials Science and Engineering. He received a National Science Foundation CAREER award in 2005 (from the Ceramics program) and an Air Force Office of Scientific Research Young Investigator award in 2007 (from the Metallic Materials program). He served as the Chair of the Basic Science Division of the American Ceramic Society (2012–2013), the Chair of the Thin Films and Interfaces committee of TMS (2012–2014), and the 2018 Chair of the Ceramics Gordon Conference. Professor Luo is a Vannevar Bush Faculty Fellow (2014–2019) and a Fellow of the American Ceramic Society (2016). Most recently, he was selected as one of the TMS 2019 Brimacombe Medalists.